RSC Advances

PAPER

View Article Online
View Journal | View Issue

Cite this: *RSC Adv.*, 2026, **16**, 12909

Interplay of defects and dopants in *l*-Dopa -aided UiO-66 for superprotonic conductivity

Powrnika Selvakumar,[a] Sathish Kumar Somu,[a] Sri Vanaja Swaminathan,[a] Amrita Pal,[b] Aneesh Anand Nechikott,[a] Prashant Kumar Nayak[a] and Tanay Kundu *[a]

Received 21st January 2026
Accepted 18th February 2026

DOI: 10.1039/d6ra00563b

rsc.li/rsc-advances

The growing demand for renewable energy sources has promoted PEMFC technology, where MOFs have emerged as an inexpensive, stable, and eco-friendly alternative to the state-of-the-art Nafion. Separate classes of functionalized and doped MOFs are explored with high conductivity in humid conditions that are per-excellent to Nafion. This work combines, for the first time, two separate approaches of (i) defect engineering and (ii) biomolecule doping. A modulator-induced defect, accompanied by doping of *l*-Dopa, a dopamine precursor, has been achieved in the D-UiO-66 backbone (LD@D-UiO-66). This dual strategy imparts superior proton conductivity (2.1×10^{-2} S cm^{-1} at 90 °C) under non-ambient conditions, surpassing that of most MOFs. Moreover, LD@D-UiO-66 exhibits a lower activation energy (0.40 eV) than D-UiO-66 (0.56 eV), showing preference towards the Grotthuss pathway through functional polar-protic sites originating from defects as well as *l*-Dopa, paving the way for MOF-based solid conductors.

1 Introduction

Over-reliance on fossil fuels to drive economic growth is leading to the perils of global warming and environmental pollution at an alarming level. Among greener energy solutions, proton exchange membrane fuel cells (PEMFCs) are the most promising technologies that convert H_2 and O_2 to H_2O and electricity. Their operating conditions are around 100 °C and 40–80% relative humidity (RH).[1] The benchmark PEM is the commercial Nafion that acts as a proton transporter and electron separator. However, its high cost, corrosive and swelling nature, degradation at lower temperature and low conductivity above 80 °C limit the fullest potential of PEMFCs. Alternative materials demand features such as cost-effectiveness, eco-friendliness, solid-state proton conductivity and thermo-mechanochemical stability over wide temperature ranges. Metal–organic frameworks (MOFs), made of metal ions/clusters and organic ligands, have established themselves as promising materials for a wide range of applications such as gas storage/separation, proton/electron carriers, catalysts and sensors. The prime advantage of MOFs is their crystallinity, porosity, and wide functionality that have yielded superior conductivity compared to Nafion.[2] In addition, the structural variety of MOFs and tailor-made modulation allow multiple treatments, such as post-synthetic modifications, defect engineering, encapsulation, and doping, providing significant scope for improvement in conductivity that is unimaginable in the case of Nafion.[3] Among promising candidates, UiO-66 ($Zr_6O_4(OH)_4(BDC)_6$), a Zr_6-cluster based MOF with a terephthalate linker, stands out as an ideal platform for separation, electrochemical biosensing, catalysis and, especially, proton conduction.[4] Currently, four routes are explored to enhance proton conductivity in MOFs; (i) by synthesizing MOFs with proton donating linkers, (ii) post-synthetic modifications of linkers in MOFs, (iii) encapsulation/doping or composite formation and (iv) defect introduction by modifying the Zr-cluster and/or by missing linker using modulators.

For example, compared to the almost insulated UiO-66, linker modification with a two-COOH group resulted in an increased conductivity of up to 0.2×10^{-2} S cm^{-1},[5] while UiO-66(NH_2) post-functionalized with an imidazole group *via* an imine bond achieved a conductivity of up to 2×10^{-2} S cm^{-1}.[6] UiO-66-COOH@PVD/PVDF composite achieved a conductivity up to 0.5×10^{-2} S cm^{-1}.[7] Modulator (acetic/stearic acid)-induced missing-linker (terephthalate) defect engineering yielded an increased conductivity up to 0.6×10^{-2} S cm^{-1}.[8] Post-synthetic modification and composite formation remain popular choices for increasing proton conduction in UiO-66 and in MOFs in general, while defect and doping approaches are very limited and scarcely explored in the literature despite showing promising results.[9–11] The main reason lies in poor thermal, mechanical as well as chemical stability after defect introduction as well as in finding suitable dopants that can

[a]*Department of Chemistry, SRM Institute of Science and Technology, Kattankulathur, Tamil Nadu, 603203, India. E-mail: ps3639@srmist.edu.in*

[b]*Department of Chemistry, Sathyabama Institute of Science and Technology, Jeppiaar Nagar, Rajiv Gandhi Salai, Chennai - 600 119, Tamil Nadu, India*

preserve structural integrity and boost application at the same time. These observations motivated us to pursue defect and doping optimization of UiO-66.[12,13]

l-Dopa ((2S)-2-amino-3-(3,4-dihydroxyphenyl)propanoic acid) is a chiral amino acid precursor for dopamine and a prescribed drug for Parkinson's disease. Apart from its biomedical significance, the polar-protic groups (catecholic –OH, $–NH_2$, –COOH) in *l*-Dopa are promising for application in nanochemistry and particularly in proton conductivity. However, it is rarely explored in nanomaterial applications, where *l*-Dopa and poly-L-Dopa are used merely as support matrices for nanoparticles.[14–16]

Herein, for the first time, *l*-Dopa has been successfully doped in missing linker defect induced D-UiO-66 (LD@D-UiO-66) and a significant improvement in proton conductivity was observed, comparable to high performing MOFs (Scheme 1). Moreover, *l*-Dopa incorporation lowers the activation energy of UiO-66 towards the Grotthuss pathway. This work marks the first time utilization of defect engineering and the incorporation of *l*-Dopa in MOFs as a dual strategy to boost proton conductivity and reduce activation energy for potential applications in PEMFCs. Although a single crystal of UiO-66 is reported without defect, most of the synthesis processes described in the literature are of polycrystalline powder form containing multiple defects such as missing Zr-cluster defect and missing organic linker defect. Compared to single crystals, these defect-induced D-UiO-66 materials are mostly used in applications due to the simplicity of setup, fast and/or inexpensive synthesis and ease of doping/composite formation. While benzoic acid and glycine are used for single crystal synthesis, HCl and formic acid are popular choices for crafting defect-induced D-UiO-66.[17] HCl introduces both missing linker defect and Zr-Cluster defect along with chloride containing impurities, while formic acid induces only missing linker defect that preserves the structural stability better, which led us to use formic acid for all the subsequent trials and optimizations.[18]

In UiO-66 synthesis, functional linker and defect installations are single-step processes, while post-synthetic modification and encapsulation follow a multistep pathway, requiring synthesis, purification, and an encapsulation/immobilization step, followed by purification. In this work, we have used a one-pot method for introducing defect/missing linker as well as immobilization of *l*-Dopa, paving the way for greener, atom-economic synthesis, saving solvent, resources and time. In a typical synthesis, 1,4-BDC, *l*-Dopa, formic acid and zirconium oxychloride are combined in a Teflon-lined autoclave heated in DMF at 110 °C for 24 h. In parallel, we have synthesized HCl mediated defect introduction. The crystallinity and structural stability are higher in the case of formic acid mediated defect installation rather than the HCl-mediated one.[19] Such an approach ensures one-step installation of missing linker defect and *l*-Dopa. The BDC: *l*-Dopa ratio has been judiciously varied (0–100) to derive the optimal product. During the trials, 7 : 3 emerged as the best material with optimal loading of *l*-Dopa and structural stability (from PXRD and TGA data). Henceforth, we proceeded with this 7 : 3 ratio for further experiments, referring to it as LD@D-UiO-66. The incorporation, interaction and bonding properties of *l*-Dopa were assessed by state-of-the-art characterization techniques.

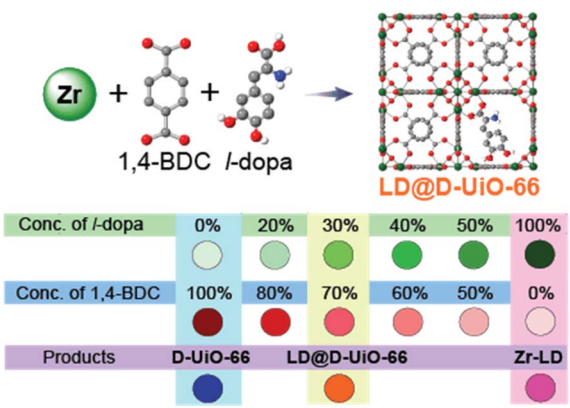

Scheme 1 Schematic of the dual strategy of defect engineering and *l*-dopa doping (top). Optimization scheme of LD@D-UiO-66 (bottom).

2 Experimental section

2.1 Materials and reagents

Terephthalic acid (1,4-BDC) and zirconium oxychloride octahydrate ($ZrOCl_2 \cdot 8H_2O$), *N*-dimethylformamide (DMF), hydrochloric acid (HCl), formic acid (HCOOH), ethanol absolute (CH_3CH_2OH) and *l*-Dopa were obtained from Loba Chemie Pvt. Ltd and were used without further purification.

2.2 Synthesis of D-UiO-66

$ZrOCl_2 \cdot 8H_2O$ (1.29 g) and 1,4-BDC (0.664 g) were dissolved in 20 mL DMF and to the solution, formic acid was added as a modulator. The clear solution obtained was heated in an oven at 110 °C for 48 h. After cooling to room temperature, the gel was collected and washed with DMF (30 mL × 3) and absolute ethanol (30 mL × 3). The next day, the colourless product was centrifuged and air-dried overnight. A colourless powder of D-UiO-66 was obtained.

2.3 High-throughput synthesis of levodopa doped D-UiO-66

Initial screening was carried out by using a high-throughput setup. Teflon of 5 mL capacity were utilized, and based on Table S1, SI, the ratios of *l*-Dopa and 1,4-BDC were varied into 9 batches to figure out the most crystalline product. Then, the bulk synthesis was carried out following the below given procedure. The better crystalline product was obtained by using $ZrOCl_2 \cdot 8H_2O$ (1.29 g), 1,4-benzenedicarboxylic acid (1,4-BDC) (0.465 g), and *l*-Dopa (0.237 g) dissolved in 20 mL DMF with formic acid as the modulator.

The transparent solution was heated in an oven at 110 °C for 48 h. At room temperature, the dark brown gel obtained from the synthesis was rinsed with DMF (30 mL × 3) and absolute ethanol (30 mL × 3). The next day, the brown product was centrifuged and air-dried overnight. A dark brown powder of LD@D-UiO-66 was obtained. Of the 9 batches, 30% of LD and 70% of 1,4-BDC showed better crystallinity, whereas 100% of LD gave an amorphous powder.

2.4 Characterization methods

Powder X-ray diffraction (PXRD) was conducted on a Davinci diffractometer using Cu-Ka radiation ranging from 5° to 90° (Bruker USA D8 Advance). Fourier transform-infrared spectroscopy (Shimadzu, IRtracer 100) was used to identify functional groups within 400–4000 cm^{-1}. The morphology of D-UiO-66 and LD@D-UiO-66 was examined using a high-resolution scanning electron microscope (HR-SEM) at 20 kV (Thermo Scientific Apreo S). EDX (energy-dispersive X-ray spectroscopy) was utilized to analyze the composition of elements on the surface (ISIS300 instrument). A JEOL JEM-2100 Plus (Japan) was used to capture the HR-TEM images of LD@D-UiO-66. Quantachrome Autosorb iQ3 surface area analyzer was used to obtain the physisorption isotherm from which the BET surface area was calculated. The instrument used for thermogravimetric analysis (TGA) was a -Netzsch STA 2500 Regulus thermogravimetric analyzer, and N_2 atmosphere was used for the studies. A PerkinElmer Phi 1600 ESCA instrument for X-ray photoelectron spectroscopy (XPS) was used to evaluate the surface elemental composition of D-UiO-66, LD@D-UiO-66 and *l*-Dopa samples.

2.5 Proton conductivity setup

D-UiO-66 and LD@D-UiO-66 samples were made into disc-like pellets (Fig. 1a and b) having approximately 0.13 mm diameter, and 1.33 mm thickness using a hydraulic press under a pressure of 100 kg cm^{-2}. A thin coating of silver paste was applied to the pellet, and then the pellet was placed in the proton conductivity setup (Fig. 1c). The electrodes were connected to the setup and the impedance was measured using a ZIVE-SP1 instrument for a frequency range of 100 kHz to 10 mHz. The humidity was monitored throughout the experiment by using a hygrometer.[20]

The proton conductivity σ (S cm^{-1}) was determined using the following equation:

$$\sigma = l/SR$$

where σ, l, S, and R represent the pellet's conductivity (S cm^{-1}), thickness (cm), cross-sectional area (cm^2), and bulk resistance (Ω), respectively. The activation energy (E_a) was determined using the following equation:

$$\ln \sigma T = \ln \sigma_0 - (E_a/KT)$$

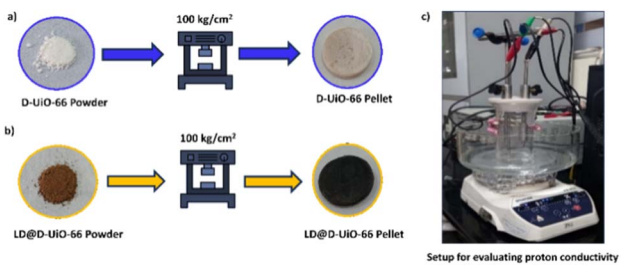

Fig. 1 (a) Pelletizing the D-UiO-66 powder. (b) Pelletizing the LD@D-UiO-66 powder. (c) Proton conductivity setup.

where σ, K, and T represent conductivity (S cm^{-1}), the Boltzmann constant (eV $K)^{-1}$, and temperature (K), respectively.

3 Results and discussion

3.1 Structural characterization of LD@D-UiO-66

The experimental PXRD pattern of LD@D-UiO-66 shows intense reflections around 7.25° and 8.39° and other reflections with comparatively lower intensities, indicating the structural integrity of parent D-UiO-66 (Fig. 2a).[21] FTIR spectra (Fig. 2b) reveal a broader peak around 3300 cm^{-1}, indicative of O–H stretching vibrations. In *l*-Dopa, the C=O stretching vibration is observed around 1652 cm^{-1}, whereas in pristine UiO-66, the C=O peak appears around 1648 cm^{-1}. In LD@D-UiO-66, the C=O peak appears at 1658 cm^{-1}, indicating a blue shift after *l*-Dopa binding. The C–H peaks in *l*-Dopa (2885, 2987 cm^{-1}) are evident in LD@D-UiO-66 with broadening, which were absent in parent D-UiO-66.[22] The Brunauer–Emmett–Teller (BET) surface area for D-UiO-66 and LD@D-UiO-66 are 1023 m^2 g^{-1} and 1044 m^2 g^{-1}, respectively (Fig. 2c). The pore size measurement with the Barrett–Joyner–Halenda (BJH) model is 1.054 cc g^{-1} for LD@D-UiO-66 and 1.033 cc g^{-1} for D-UiO-66 (Fig. 2d).[18]

Compared to D-UiO-66 with micropores (1.2, 1.4 nm) and very few mesopores, the LD@D-UiO-66 bears additional mesopores around 7.5 nm and macropores in the 50–100 nm range, proving evidence for successful missing linker defect installation in combination with formic acid and *l*-Dopa. The BET plot shows larger hysteresis for LD@D-UiO-66, indicative of macropore induced capillary-type condensation of N_2 molecules. The optical properties of the materials are interpreted using UV-DRS. LD@D-UiO-66 shows improved optical absorption as well as reduced band gap (from 3.8 eV to 3.5 eV) (Fig S1 and S2,

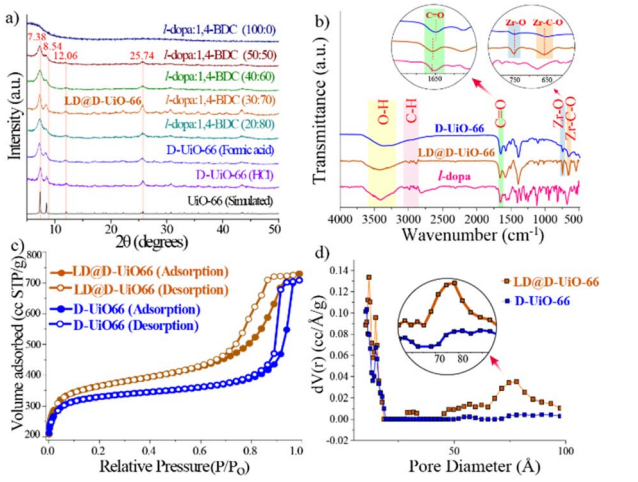

Fig. 2 (a) PXRD patterns of D-UiO-66 and LD@D-UiO-66 with different ratios of 1,4-BDC and *l*-Dopa. (b) FTIR spectra of D-UiO-66, *l*-Dopa and LD@D-UiO-66, inset on the left showing an enlarged graph corresponding to the C=O bond, inset on the right showing an enlarged graph corresponding to Zr–O and Zr–C–O bonds. (c) Adsorption and desorption curves for D-UiO-66 and LD@D-UiO-66. (d) BJH pore volume distribution for D-UiO-66 and LD@D-UiO-66 with inset highlighting the mesopore region.

SI). The possible presence of poly *l*-Dopa formation in the D-UiO-66 matrix has also been considered. Contrary to the common oxidative polymerization of amino-acid monomers, the synthesis of LD@D-UiO-66 involves a reducing-agent modulator, formic acid. During NMR sample preparation with HF, no coloured precipitate in the suspension is observed. These results collectively suggest that poly *l*-Dopa formation is unlikely, and the minute amount, even if formed, is below the detection limit of common characterization techniques. Despite due precautions, the color of LD@D-UiO-66 alludes to a negligible amount of poly *l*-Dopa formation inside the D-UiO-66 matrix. HR-SEM images reveal distorted octahedral morphology in both D-UiO-66 and LD@D-UiO-66, potentially due to the missing linker induced defects and doping of *l*-Dopa (Fig. 3a).

In TGA, the high weight loss below 100 °C for the as-synthesized MOFs is due to the entrapped and loosely bound ethanol used in the purification process. The secondary weight loss above 100 °C is due to formic acid and *l*-Dopa decomposition, followed by the framework rupture (Fig. S3, SI). The ethanol molecules are trapped in the pores during washing and are removed when the sample is pelletized.[23]

XPS analysis was performed on both D-UiO-66 and LD@D-UiO-66 in order to ascertain the nitrogen content, which can directly link to the percentage of *l*-Dopa doping. According to XPS analysis (Fig. 4), LD@D-UiO-66 shows 0.68% nitrogen, which is absent in pristine D-UiO-66.

The elemental compositions of D-UiO-66, LD@D-UiO-66, and *l*-Dopa are given in Table S2, SI. Upon considering that N originates in LD@D-UiO-66 from *l*-Dopa only, the percentage of *l*-Dopa doped in LD@D-UiO-66 = (the atomic percentage of N in LD@D-UiO-66/the atomic percentage of N in *l*-Dopa) × 100 = (0.68/4.97) × 100 = 13.68%. This agrees with the remaining total atomic percentage (86%) consisting of Zr (3.49%), C (56.96%), and O (26.36%), which corresponds to the UiO-66 framework in the literature. The number of missing linkers per Zr_6 in both D-UiO-66 and LD@D-UiO-66 is approximately 2, and the calculation is included in Table S4, SI. We have to note that the ratio of the *l*-Dopa:BDC ratio in the structure is not the same as the feeding ratio of *l*-Dopa:BDC in synthesis. This is due to BDC competing with *l*-Dopa and formic acid to coordinate with Zr^{4+}, which prohibits the coordination of *l*-Dopa with Zr^{4+}, thereby leaving *l*-Dopa to get encapsulated in the structure, and also, while synthesizing the material, during the purification process, there is loss of some *l*-Dopa which is not encapsulated/bound to the framework.

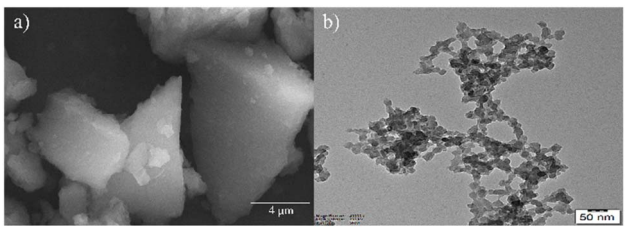

Fig. 3 (a) HR-SEM image of LD@D-UiO-66 showing a distorted octahedral morphology. (b) HR-TEM image of LD@D-UiO-66.

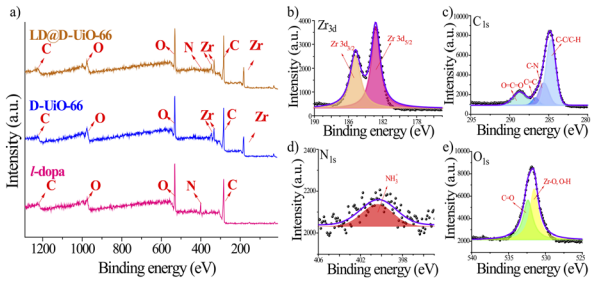

Fig. 4 (a) Full XPS spectra of LD@D-UiO-66, D-UiO-66 and *l*-Dopa. XPS spectra showing (b) Zr 3d, (c) C 1s, (d) N 1s, and (e) O 1s of LD@D-UiO-66.

3.2 Proton conductivity

We have calculated the proton conductivity of D-UiO-66 and LD@D-UiO-66 using the conventional pseudo-four-probe method. The high temperature data were collected between 25 and 90 °C, while low temperature data were gathered in the 5–25 °C range to have complete temperature-dependent conductivity of the samples (Section S8, SI). For defect-induced D-UiO-66, the ambient temperature conductivity has been observed as 5.2×10^{-4} S cm^{-1}. Upon increasing the temperature, the conductivity rises steadily, reaching the highest conductivity up to 1.6×10^{-2} S cm^{-1} at 90 °C under 98% RH.

In case of LD@D-UiO-66, the conductivity at room temperature is 1.5×10^{-3} S cm^{-1}, which is one order of magnitude higher compared to defect sites in defective clusters. Despite the presence of large macropores in LD@D-UiO-66, the water-mediated carrier channels remain unabridged and aid the superior conductivity at 90 °C of 2.1×10^{-2} S cm^{-1} at 98% RH. The proton conductivity data of LD@D-UiO-66 are comparable to most of the high performing MOFs (summarized in Fig. 5e and in Table S11, SI) which operate *via* different mechanisms. Strikingly, although functional linker, post-synthetic modification and defect induced change in conductivity have been observed, we could not find an encapsulated/doped UiO-66 proton-conducting contender for a fairer comparison, which also highlights the novelty of our investigation. The proton conductivity change was regular and reversible, proving reliability and reproducibility. In a step forward, we have measured the crystallinity of the pellets after the temperature cycles and found complete agreement of the sample with the PXRD pattern and FT-IR data before measurement. The temperature dependent conductivity data were used to calculate the Arrhenius plot for the temperature ranging from 25 to 90 °C, which reveals activation energy of 0.56 eV and 0.40 eV, respectively, for D-UiO-66 and LD@D-UiO-66 (Fig. 5d). In the literature, generally microporous MOFs show lower activation energy and higher conductivity compared to their macroporous counterparts. The large separation of protic sites and carrier molecules imposes a vehicular pathway of proton conduction in macroporous MOFs. It is surprising to observe that despite having large macropores in LD@D-UiO-66 around 50–100 nm, the *l*-Dopa exhibits lower activation energy, indicative of more facile proton transport than D-UiO-66. The combinations of acidic sites

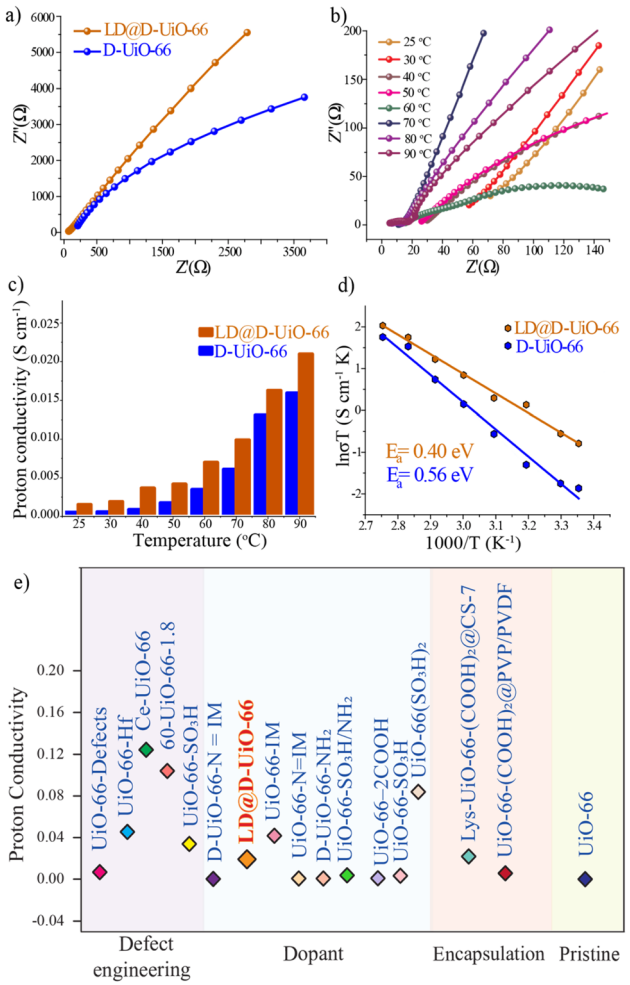

Fig. 5 (a) Nyquist plots for LD@D-UiO-66 and D-UiO-66 at room temperature (25 °C). (b) Nyquist plots for LD@D-UiO-66 for temperatures ranging from 25–90 °C. (c) Bar graph showing temperature *vs.* proton conductivity for D-UiO-66 and LD@D-UiO-66. (d) Arrhenius plots for LD@D-UiO-66 and D-UiO-66. (e) Comparative outlook of proton conductivities exhibited by pristine UiO-66, LD@D-UiO-66 and other UiO-66-derived MOFs modified by defect engineering, dopant introduction and encapsulation strategies.

originated from missing linker defect sites, as well as doped *l*-Dopa functionalities that bridge the intra- and inter-pore voids in combination with the absorbed water molecules are presumed to lower the activation energy of LD@D-UiO-66 towards a Grotthuss-type proton conduction mechanism.[21]

4 Conclusions

In conclusion, we have identified missing linker defect introduction and a protic dopant as a new dual strategy to elevate the proton conductivity of UiO-66. For this purpose, *l*-Dopa has been identified and bound to the defective Zr-cluster. In conjunction with formic acid and *l*-Dopa as modulators, one-pot synthesis of missing linker defect and doping of *l*-Dopa has been achieved successfully. Consequently, the proton conductivity of LD@D-UiO-66 increased by an order of magnitude, reaching up to 2.1×10^{-2} S cm^{-1} at 90 °C, which is comparable to most high-performing MOFs. The *l*-Dopa introduction also reduces the activation energy barrier from 0.56 eV to 0.40 eV, highlighting the importance of biomolecules in accelerating proton conductivity in ultrastable MOFs. We hope our combined strategy will empower the use of newer molecules in aiding structural modulation in advanced functional nanomaterials, especially in MOFs.

Author contributions

Powrnika Selvakumar: conceptualization, methodology, investigation, validation, writing – original draft, resources, writing -review & editing. Sathish Kumar Somu: preparation of graphical abstract, draft review & editing. Sri Vanaja Swaminathan: XPS investigation, review & editing. Amrita Pal: investigation of bandgap, UV-DRS analysis, review & editing. Aneesh Anand Nechikott: EIS review & editing. Prashant Kumar Nayak: EIS investigation, laboratory resources. Tanay Kundu: conceptualization, supervision, funding acquisition, writing-review & editing.

Conflicts of interest

There are no conflicts to declare.

Data availability

Supplementary information: synthesis of LD@D-UiO-66, UV-DRS and Tauc plot, thermogravimetric analysis (TGA), PXRD-before and after proton conductivity studies, FTIR-before and after proton conductivity studies, X-ray photoelectron spectroscopy and the elemental compositions of D-UiO-66, LD@D-UiO-66, and *l*-Dopa, calculation of percentage of missing linkers per Zr_6, proton conductivity calculation, Nyquist plots, activation energy calculation, temperature *vs* proton conductivity, relative humidity *vs.* proton conductivity at 25 °C, comparison table of LD@D-UiO-66 and Nafion, comparison table of proton conductivities of UiO-66 based MOFs with current work. See DOI: https://doi.org/10.1039/d6ra00563b.

Acknowledgements

This work is supported by the funding provided by the Science and Engineering Research Board (SERB) start-up research grant SRG/2022/002195.

Notes and references

1 M. Kiani, Y. Zhao and R. Zhang, *Chem. Commun.*, 2025, **61**, 9392–9411.
2 P. Ramaswamy, N. E. Wong and G. K. H. Shimizu, *Chem. Soc. Rev.*, 2014, **43**, 5913–5932.
3 L. Feng, H. B. Hou and H. Zhou, *Dalton Trans.*, 2020, **49**, 17130–17139.

4 J. H. Cavka, S. Jakobsen, U. Olsbye, N. Guillou, C. Lamberti, S. Bordiga and K. P. Lillerud, *J. Am. Chem. Soc.*, 2008, **130**, 13850–13851.
5 D. D. Borges, S. Devautour-Vinot, H. Jobic, J. Ollivier, F. Nouar, R. Semino, T. Devic, C. Serre, F. Paesani and G. Maurin, *Angew. Chem., Int. Ed.*, 2016, **55**, 3919–3924.
6 X. M. Li, J. Jia, M. Zhao, D. Liu, J. Gao and Y. Q. Lan, *Chem. Commun.*, 2024, **60**, 6777–6780.
7 Y. Gao, Q. Zhou, H. Xu, B. Liu, Q. Zhang, Z. Dai, S. Wang and R. Jiang, *Chem. Commun.*, 2024, **60**, 6777–6780.
8 J. M. Taylor, S. Dekura, R. Ikeda and H. Kitagawa, *Chem. Mater.*, 2015, **27**, 2286–2289.
9 V. G. Ponomareva, E. S. Shutova, K. A. Kovalenko and V. P. Fedin, *Molecules*, 2022, **27**(23), 8387.
10 S. Lin, S. A. Kedzior, J. Zhang, M. Yu, V. Saini, R. P. S. Huynh, G. K. H. Shimizu and M. Trifkovic, *Chem*, 2023, **9**, 2547–2560.
11 S. Mukhopadhyay, J. Debgupta, C. Singh, R. Sarkar, O. Basu and S. K. Das, *ACS Appl. Mater. Interfaces*, 2019, **11**, 13423–13432.
12 X. M. Li, J. Jia, M. Zhao, D. Liu, J. Gao and Y. Q. Lan, *Chem. Commun.*, 2024, **60**, 6777–6780.
13 Q. Wang, D. Shen, Z. Tu and S. Li, *Int. J. Hydrogen Energy*, 2024, **56**, 1249–1256.
14 S. A. K. Elroby, M. S. I. Makki, T. R. Sobahi and R. H. Hilal, *Int. J. Mol. Sci.*, 2012, **13**, 4321–4339.
15 A. Hamedi, M. B. Zarandi and M. R. Nateghi, *J. Environ. Chem. Eng.*, 2019, **7**(1), 102882.
16 Z. G. Gu, W. Q. Fu, M. Liu and J. Zhang, *Chem. Commun.*, 2017, **53**, 1470–1473.
17 A. Schaate, P. Roy, A. Godt, J. Lippke, F. Waltz, M. Wiebcke and P. Behrens, *Chem. Eur. J.*, 2011, **17**, 6643–6651.
18 S. Daliran, A. R. Oveisi, C. W. Kung, U. Sen, A. Dhakshinamoorthy, C. H. Chuang, M. Khajeh, M. Erkartal and J. T. Hupp, *Chem. Soc. Rev.*, 2024, **53**(12), 6244–6294.
19 M. Sanz, P. Leo, C. Palomino, M. Paniagua, G. Morales and J. A. Melero, *Green Chem.*, 2024, **26**, 7337–7350.
20 T. Kundu, S. Chandra Sahoo and R. Banerjee, *Chem. Commun.*, 2012, **48**, 4998–5000.
21 S. Tatay, S. Martínez-Giménez, A. Rubio-Gaspar, E. Gómez-Oliveira, J. Castells-Gil, Z. Dong, Á. Mayoral, N. Almora-Barrios, N. M. Padial and C. Martí-Gastaldo, *Nat. Commun.*, 2023, **14**, 6962.
22 M. H. Tran, L. C. Jheng, Z. L. Zhao, W. C. Ko, K. S. Ho and T. C. Liao, *Int. J. Hydrogen Energy*, 2024, **77**, 1375–1386.
23 A. Rapeyko, J. C. Díaz Infante and F. X. Llabrés i Xamena, *Mol. Syst. Des. Eng.*, 2023, **8**, 775–785.